

000 001 002 003 004 005 006 007 008 009 010 011 012 013 014 015 016 017 018 019 020 021 022 023 024 025 026 027 028 029 030 031 032 033 034 035 036 037 038 039 040 041 042 043 044 045 046 047 048 049 050 051 052 053 CARDIOCOMPOSER: LEVERAGING DIFFERENTIABLE GEOMETRY FOR COMPOSITIONAL CONTROL OF ANATOMICAL DIFFUSION MODELS

006 **Anonymous authors**

007 Paper under double-blind review

011 ABSTRACT

013 Generative models of 3D cardiovascular anatomy can synthesize informative struc-
014 tures for clinical research and medical device evaluation, but face a trade-off
015 between geometric controllability and realism. We propose CardioComposer: a
016 programmable, inference-time framework for generating multi-class anatomical
017 label maps based on interpretable ellipsoidal primitives. These primitives represent
018 geometric attributes such as the size, shape, and position of discrete substructures.
019 We specifically develop differentiable measurement functions based on voxel-wise
020 geometric moments, enabling loss-based gradient guidance during diffusion model
021 sampling. We demonstrate that these losses can constrain individual geometric
022 attributes in a disentangled manner and provide compositional control over multiple
023 substructures. **Finally, we show that our method is compatible with a wide array**
024 **of anatomical systems containing non-convex substructures, spanning cardiac,**
025 **vascular, and skeletal organs.**

027 1 INTRODUCTION

030 Three-dimensional segmentations of human anatomy power a variety of physics-based simulation
031 platforms. For example, virtual cohorts of anatomy can be used for virtual clinical trials to evaluate
032 and optimize novel medical devices and imaging systems Sarrami-Foroushani et al. (2021); Viceconti
033 et al. (2021); Abadi et al. (2020). Additionally, biophysical simulations can generate insights in the
034 context of both computational physiology research Niederer et al. (2020); Straughan et al. (2023);
035 Roney et al. (2020) and surgical training Yu et al. (2024). Anatomical segmentations can also be
036 used to augment machine-learning workflows through the formation of synthetic images, either
037 through imaging simulators Gopalakrishnan et al. (2024); Gopalakrishnan & Golland (2022), domain
038 randomization Dey et al. (2025); Billot et al. (2023), or generative models Fernandez et al. (2022;
2024).

039 Generative models of anatomy trained on patient-specific data offers advantages for simulation use-
040 cases. For example, conditional generation can augment computational trial cohorts with anatomical
041 variants that are both novel and rare Kong et al. (2024b). Moreover, generative editing methods,
042 such as inpainting, can precisely modify existing patient geometries to create anatomically plausible
043 variations Kadry et al. (2024; 2025). These “digital siblings” can be used with biophysical simulators
044 to model *counterfactual* scenarios that elucidate the relationship between anatomical form and
045 function.

046 However, unlike generative modeling of 3D shapes for artistic purposes, generating anatomical
047 models for biophysical simulations presents several unique challenges. The first challenge concerns
048 *scale-critical* features, in which minor geometric variations on the order of millimeters can cause
049 major fluctuations in physiological behavior Fabris et al. (2022); Sacco et al. (2018); Moore & Dasi
050 (2015). Second, anatomical structure exerts *attribute-specific* effects, in which geometric features
051 such as size and position play different roles in determining biophysical outcomes Kadry et al. (2021).
052 Third, the geometry of multiple substructures interact in a *compositional* manner Kadry et al. (2021);
053 Bhalodia et al. (2018); Kong et al. (2024a), where simulated outcomes are influenced by the collective
arrangement of various substructures. Lastly, to interface with clinicians and device engineers, such

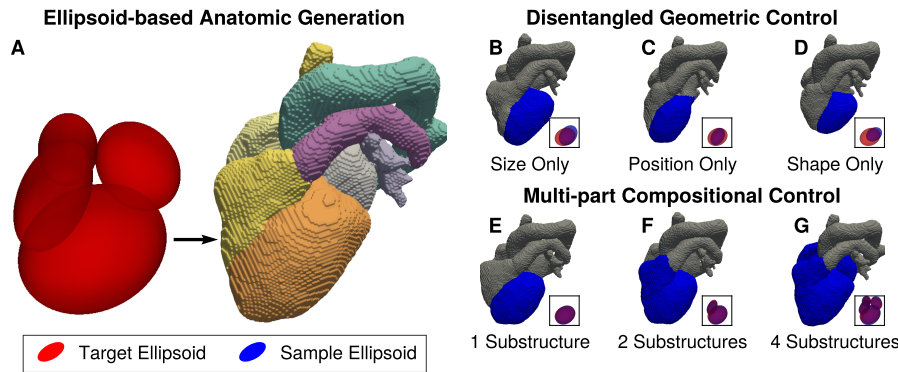


Figure 1: We present a guidance framework to constrain diffusion models of multi-label anatomical segmentations based on simple geometric features. Such features include size, shape, and position, and can be represented as ellipsoids in 3D space (panel A). Our inference-time approach enables generation based on independent geometric features (panels B-D), and supports multi-component compositional generation (panels E-G). Gray \blacksquare and blue \blacksquare voxels represent components that are unconstrained and constrained, respectively. Purple ellipsoids $\textcolor{purple}{\bullet}$ indicate a strong overlap between target $\textcolor{red}{\bullet}$ and sample ellipsoids $\textcolor{blue}{\bullet}$.

generative models should be controllable via primitives that are interpretable and physiologically relevant.

To address these design requirements, we present CardioComposer, an energy-based guidance framework for controlling unconditional diffusion models with geometric attributes regarding size, shape, and position. We visually represent these constraints via interpretable ellipsoidal primitives (Figure 1 A). Our inference-time framework can independently control individual attributes such as size or position (Figure 1 B-D), and compose geometric constraints for an arbitrary number of anatomical components or substructures (Figure 1 E-G). Our *key insight* is that unconditional diffusion models of multi-class anatomy can be constrained in a compositional manner by simple gradients derived from geometric loss functions applied individually to each substructure. We demonstrate this method on multi-tissue cardiovascular segmentations that exhibit a wide array of substructures such as star-shaped chambers and tubular vasculature. Our framework advances the state of the art in the following ways:

- **Differentiable Geometry for Anatomical Characterization:** We introduce a set of differentiable geometric measurement functions that compute physiologically relevant anatomical features from a substructure label map. We specifically measure voxel-wise geometric moments compute size via zeroth-order moments, position via first-order moments, and shape via scale-normalized second-order moments.
- **Inference-time Guidance to Control Substructure Geometry:** We demonstrate that simple gradients derived from differentiable geometric loss functions can guide unconditional latent diffusion models of discretized multi-class label maps. This enables *independent* or *joint* control of substructure attributes without retraining, where substructures consist of one tissue class or the union of multiple classes.
- **Complex Compositional Control:** We validate that multiple substructure-specific geometric losses can be composed to enable more complex anatomical constraints. Further, we show that this control extends to non-convex substructures with branching or curved geometry.

2 BACKGROUND

Traditional Morphometric Modeling for Anatomy. Morphometry involves quantifying anatomical structure through geometric measurements. Traditional morphometric approaches measure intrinsic features such as length, area, volume, and shape, as well as extrinsic factors such as position and orientation. Geometric measurements enable applications such as cardiovascular risk stratification

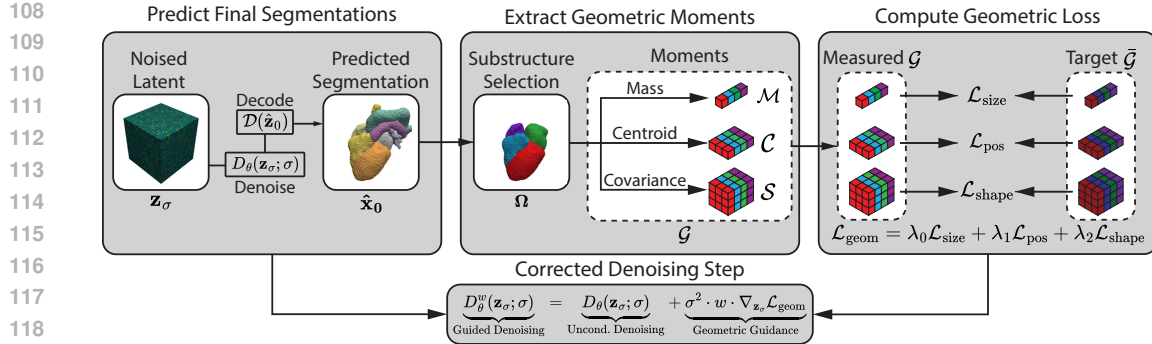


Figure 2: **Our method involves applying a geometric guidance correction step for every denoising iteration.** Left: The noised latent z_σ is passed through the diffusion model and VAE decoder to produce a clean voxel space prediction \hat{x}_0 (Section 4.2). Middle: The segmentation is parsed for relevant substructures Ω , and geometric moments \mathcal{G} are extracted for each substructure (Section 4.3). Right: Measured geometric moments \mathcal{G} are compared to target moments $\bar{\mathcal{G}}$ through geometric moment losses. Bottom: The gradient derived from the aggregate loss corrects the denoising step.

Asheghan et al. (2023); Mahmud et al. (2024) and orthopedic diagnosis Gatti et al. (2024). However, traditional morphometric approaches face two key challenges: they cannot represent complex relationships between features, and multiple distinct anatomies may map to the same high-level measurements. To address these limitations, we propose a framework in which an unconditional diffusion model is controlled by traditional morphometric features (size, shape, and position) to generate a variety of realistic anatomical structures, providing an approachable anatomical modeling interface for both clinical and engineering workflows involving numerical simulation.

Generative Models for Numerical Simulation. Anatomical models in the form of 3D meshes or label maps, serve as a crucial tool for studying form-function relationships through physical simulations, enabling both scientific discovery and medical device design. However, current approaches to create such models must trade off between *fidelity* and *control*. Simple geometric primitives, such as cylinders for coronary arteries Madani et al. (2019) and truncated ellipsoids for cardiac chambers Aróstica et al. (2025) offer parametric control but fail to capture anatomical realism. Data-driven approaches such as autoencoders Dou et al. (2022); Qiao et al. (2025) represent anatomy in terms of global shape vectors, and can generate synthetic data for mechanistic studies of heart disease Hermida et al. (2024); Williams et al. (2022). However, such approaches are limited in their ability to model *interpretable* geometric attributes. Deformation editing methods Pham et al. (2023; 2024) allow for interpretable control of anatomical geometry, but are limited to modifying existing models. Recently, diffusion-based approaches such as inpainting and partial diffusion have been used to edit patient-specific anatomy to create “digital siblings” Kadry et al. (2024). However, such edits can induce undesirable morphological bias when applied to rare and pathological cases. To this end, recent studies have imposed anatomical features by explicitly providing scalar conditioning features during training. For example, de Wilde et al. (2025) trained a conditional model on thyroid segmentations, and Kadry et al. (2025) introduced morpho-skeletal conditioning and guidance mechanisms for coronary arteries. However, both approaches rely on conditional training and are restricted to size-related variables such as volume or cross-sectional area. **Similarly, Du et al. (2025) presented a hierarchical conditional diffusion model for generating aortic centerlines and radial profiles, but is restricted to fixed centerline connectivity and cannot flexibly accommodate topological changes such as varying branching patterns.** In contrast, we propose a modular inference-time framework that controls *unconditional* diffusion models across diverse anatomical structures using geometric attributes such as size, shape, and position.

Spatial Control of Generative Models. Spatial control of generative models is achieved through two principal approaches. The first approach conditions models on interpretable mid-level representations (e.g., bounding boxes, ellipsoid parameters, **articulation angles**) and has been successfully applied to images Nie et al. (2024), video Feng et al. (2025), 3D objects Hertz et al. (2022); Koo et al. (2023); Mu et al. (2021), and proteins Stark et al. (2025). However, these methods cannot accommodate

novel constraints without retraining. The second approach employs energy-based guidance during the reverse diffusion process Bansal et al. (2023); Du et al. (2023), enabling flexible constraint composition at test time, but is typically limited to general localization rather than exact geometric control. Recent works such as self-guidance use attention-based loss functions to enable basic geometric attribute control (size, position) in text-to-image models Epstein et al. (2023), but is not designed for multi-label segmentations, nor does it control for orientation or aspect ratio. In our work, we extend energy-based guidance by introducing differentiable geometric losses for 3D multi-component anatomical voxel maps based on substructure-specific geometric properties such as the mass, centroid, and covariance, enabling the composition of multiple constraints across several independent substructures.

3 ANATOMICAL DIFFUSION MODELS

Let $\mathbf{x} \in \mathbb{R}^{C \times H \times W \times D}$ be a 3D segmentation volume with C tissue channels and (H, W, D) spatial dimensions. We employ a variational autoencoder (VAE) with an encoder \mathcal{E} that maps \mathbf{x} to a lower-dimensional latent representation $\mathbf{z} = \mathcal{E}(\mathbf{x})$, and a decoder \mathcal{D} that maps \mathbf{z} back to voxel space reconstruction $\tilde{\mathbf{x}} = \mathcal{D}(\mathbf{z})$. The latent grid $\mathbf{z} \in \mathbb{R}^{c \times h \times w \times d}$ comprises c channels and spatial dimensions $(h, w, d) = (H/f, W/f, D/f)$ for an integer downsampling factor f .

We use an unconditional latent diffusion model (LDM) as a prior over 3D anatomical segmentations, trained on the encoded latent representations \mathbf{z} . We specifically use the elucidated diffusion formulation of Karras et al. (2022). In the forward process, data samples $\mathbf{z} \sim p_{\text{data}}(\mathbf{z})$ are progressively corrupted by adding Gaussian noise, yielding in perturbed data $\mathbf{z}_\sigma = \mathbf{z} + \mathbf{n}$ where $\mathbf{n} \sim \mathcal{N}(\mathbf{0}, \sigma^2 \mathbf{I})$. The reverse process reconstructs the original data by approximating the score function $\nabla_{\mathbf{z}_\sigma} \log p(\mathbf{z}_\sigma; \sigma)$ that controls the reverse diffusion process:

$$d\mathbf{z}_\sigma = -2\sigma \nabla_{\mathbf{z}_\sigma} \log p(\mathbf{z}_\sigma; \sigma) dt + \sqrt{2\sigma} d\mathbf{w} \quad (1)$$

where $d\mathbf{w}$ is the Wiener process. This score function $\nabla_{\mathbf{z}_\sigma} \log p(\mathbf{z}_\sigma; \sigma) = (D_\theta(\mathbf{z}_\sigma; \sigma) - \mathbf{z}_\sigma)/\sigma^2$ can be expressed via a denoising function D_θ parametrized by a 3D U-Net F_θ through the following relation:

$$D_\theta(\mathbf{z}_\sigma; \sigma) = c_{\text{skip}}(\sigma) \mathbf{z}_\sigma + c_{\text{out}}(\sigma) F_\theta(c_{\text{in}}(\sigma) \mathbf{z}_\sigma; c_{\text{noise}}(\sigma)). \quad (2)$$

Where $(c_{\text{skip}}, c_{\text{out}}, c_{\text{in}}, c_{\text{noise}})$ are noise-level-dependent scaling coefficients. The neural network is trained by minimizing the clean-data prediction objective $L = \mathbb{E}_{\sigma, \mathbf{z}, \mathbf{n}} [\lambda(\sigma) \|D_\theta(\mathbf{z}_\sigma; \sigma) - \mathbf{z}\|_2^2]$, with $\lambda(\sigma)$ balancing loss contributions across noise levels.

4 GEOMETRIC GUIDANCE

4.1 OVERVIEW

Our objective is to guide an unconditional diffusion model that synthesizes anatomical segmentations with geometric constraints for size, position, and shape. These attributes are measured on substructures that correspond to discrete tissue labels within the 3D voxel map. To do this, we guide the sampling process with a composite *geometric loss* applied to a subset of labels. This geometric loss is a weighted sum of moment-based terms: size via zeroth-order moments (scalar volumes), position via first-order moments (centroid vectors), and shape via scale-invariant second-order moments (normalized covariance matrices). Figure 2 illustrates four main stages. First, at each sampling step we denoise the latent, decode to voxel-space logits, and apply a softmax to obtain class probabilities. Second, we select the desired anatomical substructures Ω and extract the geometric moments $\mathcal{G} = [\mathcal{M}, \mathcal{C}, \mathcal{S}]$, representing the mass, centroid, and covariance for each substructure. Third, we compute the geometric loss $\mathcal{L}_{\text{geom}}$ with respect to target moments $\bar{\mathcal{G}}$. Lastly, the gradient of this loss with respect to the noisy latents is used to guide the sampling process.

4.2 SEGMENTATION DENOISING AND GUIDANCE

We formulate loss-based guidance in terms analogous to diffusion posterior sampling Chung et al. (2023), where the gradient derived from a differentiable geometric loss $\mathcal{L}_{\text{geom}}$ guides the sampling

process. To guide anatomical generation, the intermediately noised latent \mathbf{z}_σ is denoised by the diffusion model to produce a clean prediction $\hat{\mathbf{z}}_0 = D_\theta(\mathbf{z}_\sigma; \sigma)$ and subsequently decoded into a voxel-space segmentation $\hat{\mathbf{x}}_0 = \mathcal{D}(\hat{\mathbf{z}}_0)$. As the decoder outputs are continuous logits, we apply a label-wise softmax to ensure that the segmentation values are close to binary. The geometric loss $\mathcal{L}_{\text{geom}}$ is then computed in a differentiable manner to update the denoiser predictions through the gradient with respect to the noised latent \mathbf{z}_σ . The update step is parameterized with a guidance weight w as follows:

$$\underbrace{D_\theta^w(\mathbf{z}_\sigma; \sigma)}_{\text{Guided Denoising}} = \underbrace{D_\theta(\mathbf{z}_\sigma; \sigma)}_{\text{Uncond. Denoising}} - \underbrace{\sigma^2 \cdot w \cdot \nabla_{\mathbf{z}_\sigma} \mathcal{L}_{\text{geom}}}_{\text{Geometric Guidance}} \quad (3)$$

4.3 GEOMETRIC MOMENT LOSS

To isolate guidance to specific substructures representing individual tissues, we map the input segmentation $\hat{\mathbf{x}}_0 \in \mathbb{R}^{C \times H \times W \times D}$ to a set of substructure voxel maps $\Omega \in \mathbb{R}^{E \times H \times W \times D}$. Here, E specifies the number of relevant substructures. Substructures are determined either through taking subsets of the tissue channels or taking the Boolean union of multiple tissue channels.

To extract geometric features, we compute the set of geometric moments $\mathcal{G} = [\mathcal{M}, \mathcal{C}, \mathcal{S}]$, where $\mathcal{M} \in \mathbb{R}^{E \times 1}$ represents the masses or volumes for each substructure, $\mathcal{C} \in \mathbb{R}^{E \times 3}$ represents the centroids, and $\mathcal{S} \in \mathbb{R}^{E \times 3 \times 3}$ represents the covariances. Specifically, for each individual substructure index k , we define $\Omega_k \in \mathbb{R}^{(H \times W \times D) \times 1}$ as the flattened substructure voxel grid and $\mathbf{p} \in \mathbb{R}^{(H \times W \times D) \times 3}$ as the normalized voxel coordinates between 0 and 1. We compute the geometric moments as

$$\mathcal{M}_k = \mathbf{1}^T \cdot \Omega_k \quad \text{and} \quad \mathcal{C}_k = \frac{\Omega_k^T \mathbf{p}}{\mathcal{M}_k} \quad \text{and} \quad \mathcal{S}_k = \frac{1}{\mathcal{M}_k} \mathbf{p}^T \text{diag}(\Omega_k) \mathbf{p} - \mathcal{C}_k^T \mathcal{C}_k \quad (4)$$

where $\mathbf{1}^T$ is the all-ones vector, and $\text{diag}(\cdot)$ refers to diagonal matrix embedding. To enable independent control over size and shape characteristics, we compute a normalized representation of the covariance matrix. The scale-normalized covariance matrix is defined as $\mathcal{S}_k^n = \mathcal{S}_k / \text{tr}(\Lambda)$ where Λ is the eigenvalue matrix obtained from the eigendecomposition of \mathcal{S}_k . Intuitively, the normalized covariance matrix represents the aspect ratio and orientation of the substructure.

Following the computation of geometric moments, we calculate individual loss terms by comparing each moment to its corresponding target moment $\bar{\mathcal{G}} = [\bar{\mathcal{M}}, \bar{\mathcal{C}}, \bar{\mathcal{S}}^n]$. For each geometric feature, we compute the mean squared error (MSE) between the measured and target values. These individual loss terms are defined as:

$$\mathcal{L}_{\text{size}} = \mathcal{L}_{\text{MSE}}(\mathcal{M}, \bar{\mathcal{M}}), \quad \mathcal{L}_{\text{pos}} = \mathcal{L}_{\text{MSE}}(\mathcal{C}, \bar{\mathcal{C}}), \quad \mathcal{L}_{\text{shape}} = \mathcal{L}_{\text{MSE}}(\mathcal{S}^n, \bar{\mathcal{S}}^n). \quad (5)$$

Using prescribed weight factors $\lambda_0, \lambda_1, \lambda_2$, we compute the aggregate geometric loss as $\mathcal{L}_{\text{geom}} = \lambda_0 \mathcal{L}_{\text{size}} + \lambda_1 \mathcal{L}_{\text{pos}} + \lambda_2 \mathcal{L}_{\text{shape}}$. The weighted sum of individual weights λ_i allow us to control the contribution of individual loss to the guidance process, enabling easy disentangled control by zeroing out the associated weighting factor.

5 EXPERIMENTS

5.1 UNCONDITIONAL MODEL TRAINING

For diffusion training, we use the label maps provided in the TotalSegmentator dataset Wasserthal et al. (2023). We extract heart related labels, which include aorta (Ao), pulmonary artery (PA), pulmonary veins (PV), inferior vena cava (IVC), superior vena cava (SVC), left atrium (LA), right atrium (RA), left ventricle (LV), and right ventricle (RV), and left ventricular myocardium (Myo). We manually filter out low-quality label maps, resulting in 596 3D cardiac segmentations with 11 channels and an isotropic voxel edge length of 2 mm. See Section 8.2 for further details. We split the dataset into training and validation sets with an 80/20 split. All target moments and evaluation metrics are computed on the validation set.

We train an unconditional diffusion model on cardiac label maps similarly to Kadry et al. (2024) (further details in Section 8.3). To compute our geometric guidance loss, we use the weighted sum of the individual geometric moment losses, where the guidance weights λ_i are tuned experimentally (see Section 8.4).

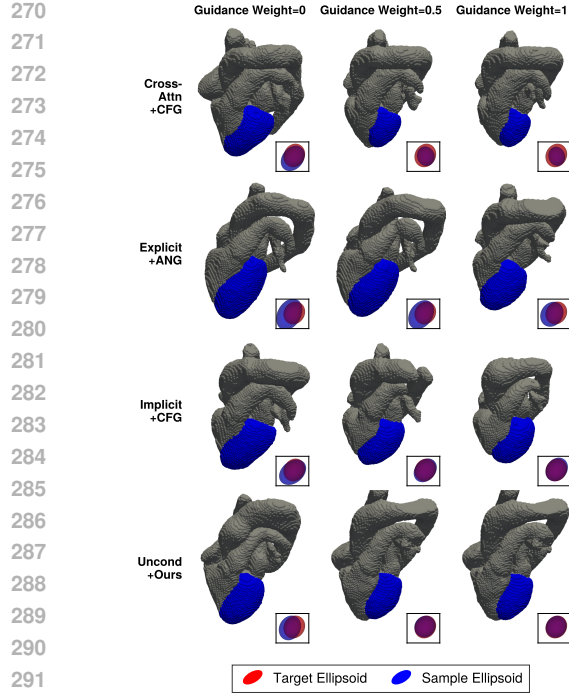


Figure 3: **Geometric guidance can generate synthetic anatomy with geometric constraints.** Grid shows example synthetic label maps where constraints are applied to the myocardium voxels. **Rows:** baseline conditioning and guidance methods (CFG = classifier-free guidance, ANG = adaptive null guidance).

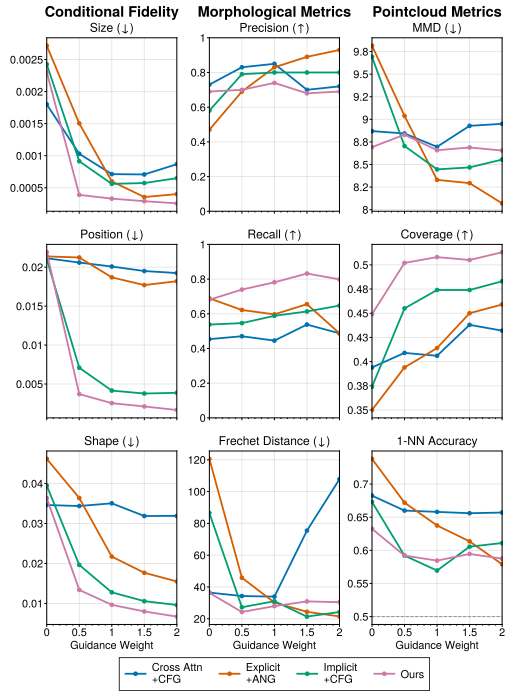


Figure 4: **Geometric guidance can enforce conditional fidelity while maintaining realism.** Line plots compare conditioning and guidance mechanisms based on the geometric properties of the myocardium. MMD values are multiplied by 10^3 .

5.2 BASELINES

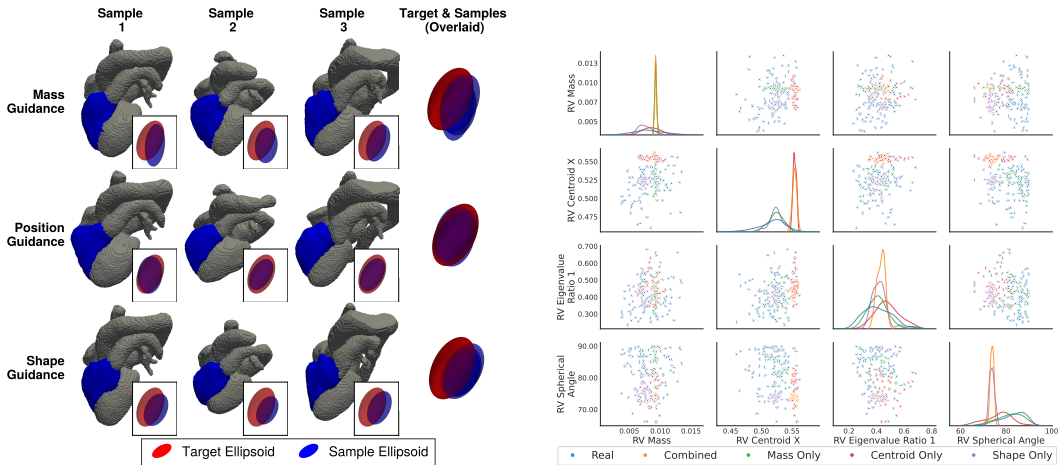
We compare our approach (unconditional diffusion combined with geometric guidance) to conditional training approaches. Given the target geometric moments representing the size \mathcal{M} , centroid \mathcal{C} and covariance \mathcal{S} of each cardiac substructure, we condition the model in the following ways:

- **Explicit Concatenation:** We directly encode geometric attributes as scalar values in the conditioning signal Kadry et al. (2025). Here, we adapt this method to positional and shape-based features. We flatten and stack all geometric moments into a 13-dimensional vector for all E substructures. We then expand this vector into a voxel grid $\mathcal{G}_{\text{exp}} \in \mathbb{R}^{13 \times E \times h \times w \times d}$ which is concatenated to the latents along the channel dimension.
- **Implicit Concatenation:** We indirectly encode geometric attributes in the conditioning signal through 3D heatmaps Kadry et al. (2025). Here, we embed geometric moments as 3D Gaussians in voxel space. For each substructure, we create a voxel map $\mathcal{G}_{\text{imp}} \in \mathbb{R}^{E \times h \times w \times d}$ where the voxel values encode the Mahalanobis distance.
- **Cross-attention:** We express the conditioning signal as a sequence of tokens where each token represents substructure geometry. The dimension of each token corresponds to the embedded geometric moments $\mathcal{G}_{\text{cross}} \in \mathbb{R}^{E \times 256}$. To enable sequence conditioning for the denoising U-Net, we convert the self-attention layers to cross-attention layers, similar to Rombach et al. (2022).

We implement guidance mechanisms such as adaptive null guidance (ANG) Kadry et al. (2025) for explicit concatenation, and classifier-free guidance (CFG) Ho & Salimans (2022) for implicit concatenation and cross-attention. Further details can be found in Section 8.5.

324 5.3 EVALUATION METRICS
325

326 We evaluate pairwise conditional fidelity for size, shape, and position by taking the L_1 -norm between
327 the target and sample moments. We measure morphological quality metrics by comparing the
328 distribution of real and synthetic anatomy in morphological feature space Kadry et al. (2024).
329 To embed each label map, we consider all 10 tissues as substructures and concatenate, over all
330 substructures, the masses, centroids, and eigenvalues of the normalized covariance matrices. We
331 specifically use morphological variants of improved precision and recall, as well as the Fréchet
332 distance (FD) Kynkänniemi et al. (2019); Kadry et al. (2024). Lastly, we leverage pointcloud-based
333 metrics to assess 3D shape Yang et al. (2019), such as minimum matching distance (MMD), coverage
334 (COV), and 1-nearest neighbor accuracy (1-NNA). Distances between pointclouds are computed with
335 Earth Mover’s Distance (EMD). Further details can be found in Section 8.6.
336



351 **Figure 5: Geometric guidance enables inde-
352 pendent control of size, shape, and position.**
353 Columns show synthetic label maps generated
354 by geometric guidance applied to the right ven-
355 tricle voxels ■ using various geometric losses.
356 Rows represent which geometric feature is being
357 independently controlled.

359 5.4 EVALUATING ANATOMICAL GENERATION QUALITY
360

361 We first aim to compare
362 and evaluate geometric con-
363 trol methods on both con-
364 ditional fidelity and syn-
365 thetic anatomy quality. We
366 sample target moments for
367 a single substructure (my-
368 ocardium) from the valida-
369 tion set and generate 200
370 anatomical segmentations
371 per method. We sweep
372 over guidance weights $w \in$
373 $[0, 2]$. In Figure 4, we show
374 that geometric guidance en-
375 hances conditional fidelity,
376 especially at higher guid-
377 ance weights. We observe that our method maintains generation quality, retaining similar levels of
378 morphological and pointcloud evaluation metrics with increasing guidance. Figure 3 shows example
379 label maps generated through varying guidance values for all methods, across guidance values for

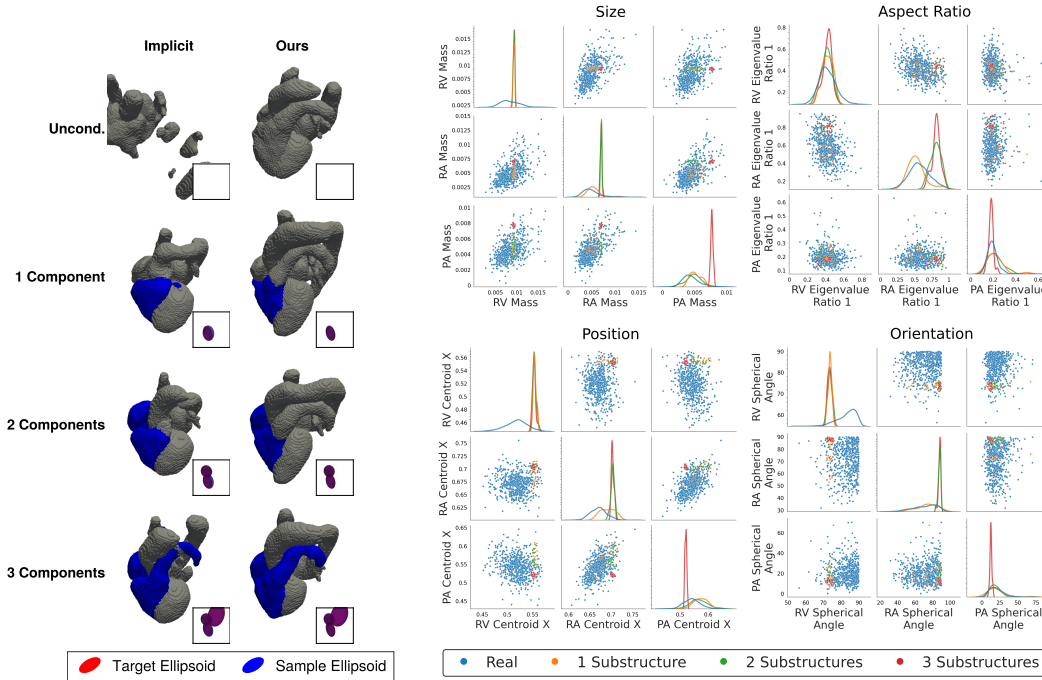
Table 1: Comparative analysis of various approaches for multi-substructures
compositional generation. The number of substructures indicates the number
of tissues actively constrained during sampling. MMD values are multiplied
by 10^3 .

Constraints	Method	Morph. Metrics			Pointcloud Metrics		
		FD (↓)	Pr. (↑)	Re. (↑)	MMD (↓)	COV (↑)	1-NNA
0	Implicit	1622	0.00	0.99	55.7	0.288	0.915
	Ours	34.6	0.70	0.87	9.40	0.53	0.55
1	Implicit	227	0.00	0.87	17.1	0.40	0.79
	Ours	38.5	0.60	0.83	9.39	0.52	0.57
3	Implicit	29.8	0.80	0.81	9.21	0.48	0.58
	Ours	32.7	0.78	0.94	8.60	0.58	0.52
6	Implicit	31.1	0.82	0.95	8.11	0.56	0.50
	Ours	35.5	0.80	0.94	8.50	0.58	0.50

378 all methods; only our method and implicit conditioning align the target and sample ellipsoids under
 379 guidance. Further information on which features were plotted can be found in Section 8.13.
 380

381 5.5 EVALUATING GEOMETRIC DISENTANGLEMENT

383 We next show that our guidance framework uniquely enables disentangled control of geometric
 384 attributes. We use 100 target moments for myocardial labels from the validation set using no losses
 385 (Uncond.), a combination of all losses ($\mathcal{L}_{\text{geom}}$), or each individual moment loss ($\mathcal{L}_{\text{size}}$, \mathcal{L}_{pos} , and
 386 $\mathcal{L}_{\text{shape}}$). Figure 9 shows that each individual loss improves its corresponding conditional-fidelity
 387 metric while leaving the others approximately unchanged. The main exception is the interaction
 388 between shape and mass, where adding a guidance weight for the shape loss enhances mass fidelity.
 389 This phenomenon is likely due to correlation of size and shape in the dataset. Qualitative results can
 390 be seen in Figures 5 and 6, where the right ventricle is constrained independently by mass, position,
 391 or shape. **For example, mass-only guidance produces a narrow peak in the mass marginal while**
 392 **the other morphology metrics remain broad, whereas applying all geometric losses collapses all**
 393 **marginals to narrow peaks at their target values.**



416 **Figure 7: Geometric guidance ex-
 417 hibits enhanced multi-part com-
 418 positional generation compared to
 419 a conditional drop-out baseline.**
 420 **Columns:** Baseline vs. our method.
 421 **Rows:** Synthetic label maps with a
 422 varying number of voxel labels ■.

424 5.6 EVALUATING MULTI-PART COMPOSITIONALITY

426 We evaluate the ability of our method to achieve multi-part control under arbitrary constraints. We
 427 sample 100 target moment sets from the validation set and constrain generation based on: (a) only
 428 the myocardium (1 substructure), (b) the right heart labels (3 substructures), and (c) both right
 429 and left heart labels (6 substructures). For geometric guidance, we use an unconditional model
 430 and select the appropriate substructures Ω during guidance. For our baseline, we retrain the best
 431 conditional diffusion model (implicit) with 6 substructures using dropout (further details can be found
 in Section 8.6). Results are shown in Table 1 and Figure 7, which show that with a small number of

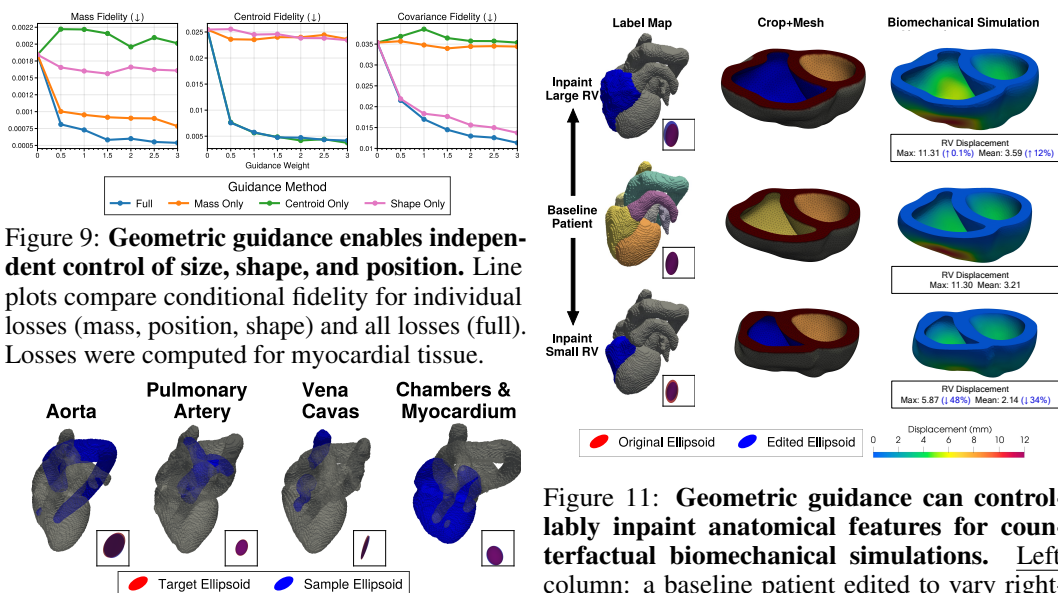
416 **Figure 8: Our guidance framework enables multi-part
 417 compositional generation.** Pair plot shows kernel density
 418 estimate plots (diagonals) and pairwise scatterplots (off-
 419 diagonals) for various morphological metrics. Guidance
 420 is applied to control the geometry for a varying number of
 421 substructures.

432 constrained substructures, implicit conditioning with dropout fails to generate high-quality anatomy
 433 as measured by morphological and pointcloud metrics. Because the implicit conditional baseline is
 434 trained with independent dropout over six ellipsoidal conditioning channels, the fully conditioned case
 435 (all channels present) is vastly more frequent than the unconditional case (all channels empty). As a
 436 result, unconditional sampling corresponds to the rarest training configuration and yields degraded
 437 anatomical quality in Figure 7 and Table 1.

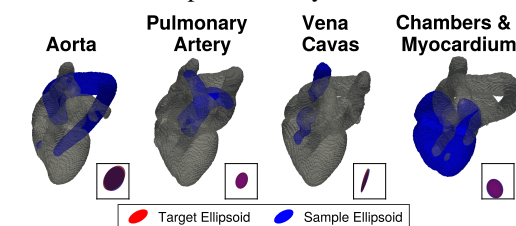
438 We further show in Figure 8 that controlling multiple substructures via geometric guidance can
 439 effectively sample from lower-dimensional slices of the original morphological distribution. For
 440 instance, when guidance is applied to a single substructure, the pair plots show a sharp concentration
 441 around the target value for the right ventricle, while the remaining structures retain broad distributions.
 442 When three substructures are guided simultaneously, the corresponding morphological marginals
 443 all collapse to narrow peaks at their target geometric values. Finally, Figure 10 shows that our
 444 guidance framework applies to complex, non-star-shaped geometries, including curved and branching
 445 substructures, as well as Boolean unions involving multiple tissue classes considered as a single
 446 substructure (e.g., both vena cavae or all chambers).

447 5.7 GEOMETRIC INPAINTING AND BIOPHYSICAL SIMULATIONS

449 We demonstrate that our geometric guidance framework can controllably edit patient-specific anatomy
 450 for simulation experiments. We consider an example involving biventricular pressurization in which
 451 we edit a label map to enlarge or shrink the RV. As shown in Figure 11, we define the RV target
 452 geometry by doubling or halving the mass measured from the original label map (left column insets).
 453 We apply tissue-based inpainting Kadry et al. (2024) with geometric guidance to edit the RV (left
 454 column) and convert the label map to a tetrahedral mesh (middle column). We simulate biventricular
 455 pressurization for the baseline patient and edited variants, showing how RV volume modulates wall
 456 displacement (right column). Further details can be found in Section 8.7.



457
 458 Figure 9: **Geometric guidance enables independent control of size, shape, and position.** Line
 459 plots compare conditional fidelity for individual losses (mass, position, shape) and all losses (full).
 460 Losses were computed for myocardial tissue.
 461



462
 463 Figure 10: **Geometric guidance is compatible
 464 with complex substructures.** Qualitative results
 465 showing geometric control of substructures with
 466 non-convex or branched features, as well as sub-
 467 structures comprising multiple tissues.
 468

481 5.8 GENERALITY OVER ANATOMICAL SYSTEMS AND STRUCTURES

482 We aim to show that geometric guidance can control unconditional diffusion models trained on a wide
 483 variety of anatomical systems. To this end, we construct and utilize three datasets of 3D multi-class
 484 patient-specific label maps: one for the branched ascending aorta, one for the spinal vertebral column,

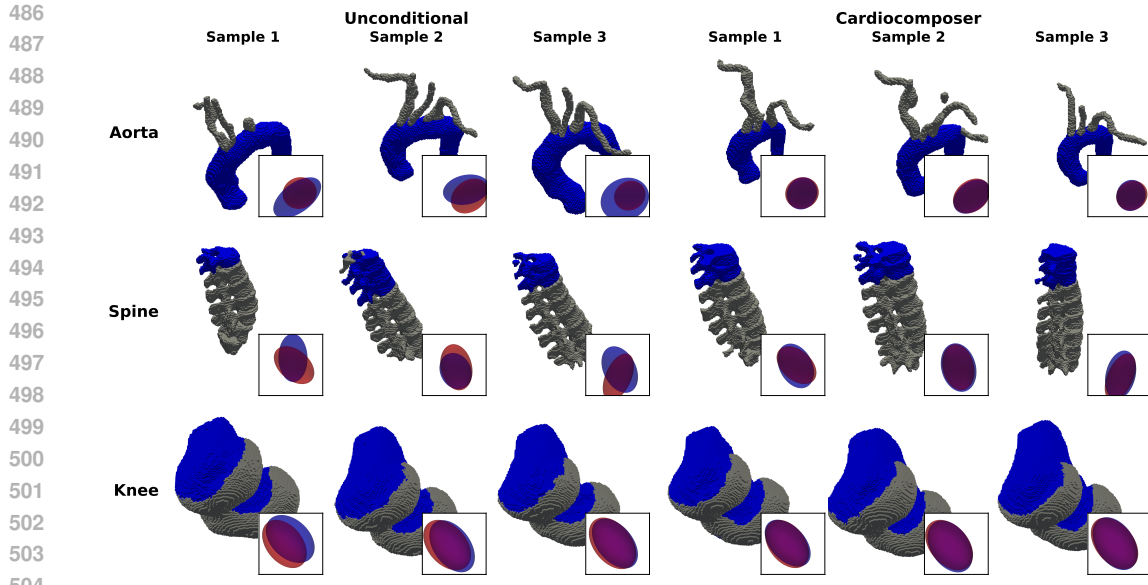


Figure 12: **Geometric guidance can control the generation of a wide variety of anatomical systems.** We present label maps that were generated from a unconditional and guided latent diffusion models. We train a separate diffusion model for each anatomical dataset. For the aortic dataset, we control the main trunk, for the spinal dataset, we control the sixth, seventh, and eighth thoracic vertebrae, while for the knee dataset, we control the femur.

and one for the distal femur comprising the femoral condyles and their articular cartilage, without the patella or tibia. Further details can be found in Section 8.2. In Figure 12, we show typical unconditional samples which do not correspond to the target geometry, as well as samples from geometric guidance, which controls substructure geometry to a high degree of fidelity.

6 LIMITATIONS

Our method has several limitations, for example, the relative weights of the geometric moments should be obtained through experimental tuning, similar to all guidance frameworks. However, we found that the same set of loss weightings transfer well to entirely different anatomical systems such as the aorta, spinal column, and knee, indicating that only minimal additional tuning is required. Moreover, substructures are currently defined based on label map class, and cannot represent sub-class localized features such as cross sections. This can be addressed by developing localized substructure selection methods, which would enable the control of localized geometric attributes. Lastly, anatomical diffusion models can generate topologically incorrect substructures-such as disconnected aortas or several left atria, making the resulting simulation physics inaccurate. This can be addressed by filtering out topologically incorrect anatomies, at the cost of some wasted computation.

7 CONCLUSIONS

We present a flexible method to impose geometric constraints on diffusion models of 3D multi-class anatomical label maps. By measuring geometric moments relating to size, shape, and position of various substructures during inference, we enable energy-based guidance without conditional training. We show that our framework can independently control geometric attributes such as size, position, or shape, and constrain multiple anatomical substructures in a compositional manner. We also demonstrate geometric guidance across a wide range of anatomical systems and structures, spanning cardiac, vascular, and skeletal systems. Our framework enables custom-tailoring realistic anatomy for computational simulation experiments, elucidating the causal relationships between form and simulated function.

540 REFERENCES
541

542 Ehsan Abadi, William P Segars, Benjamin MW Tsui, Paul E Kinahan, Nick Bottenus, Alejandro F
543 Frangi, Andrew Maidment, Joseph Lo, and Ehsan Samei. Virtual clinical trials in medical imaging:
544 a review. *Journal of Medical Imaging*, 7(4):042805–042805, 2020.

545 Reidmen Aróstica, David Nolte, Aaron Brown, Amadeus Gebauer, Elias Karabelas, Javiera Jilberto,
546 Matteo Salvador, Michele Bucelli, Roberto Piersanti, Kasra Osouli, et al. A software benchmark for
547 cardiac elastodynamics. *Computer Methods in Applied Mechanics and Engineering*, 435:117485,
548 2025.

549 Mohammad Mostafa Asheghian, Hoda Javadikasgari, Taraneh Attary, Amir Rouhollahi, Ross
550 Straughan, James Noel Willi, Rabina Awal, Ashraf Sabe, Kim I de la Cruz, and Farhad R Nezami.
551 Predicting one-year left ventricular mass index regression following transcatheter aortic valve re-
552 placement in patients with severe aortic stenosis: A new era is coming. *Frontiers in Cardiovascular
553 Medicine*, 10:1130152, 2023.

554 Arpit Bansal, Hong-Min Chu, Avi Schwarzschild, Soumyadip Sengupta, Micah Goldblum, Jonas
555 Geiping, and Tom Goldstein. Universal guidance for diffusion models. In *Proceedings of the
556 IEEE/CVF Conference on Computer Vision and Pattern Recognition*, pp. 843–852, 2023.

557 Riddhish Bhalodia, Shireen Y Elhabian, Ladislav Kavan, and Ross T Whitaker. Deepssm: a
558 deep learning framework for statistical shape modeling from raw images. In *Shape in Medical
559 Imaging: International Workshop, ShapeMI 2018, Held in Conjunction with MICCAI 2018,
560 Granada, Spain, September 20, 2018, Proceedings*, pp. 244–257. Springer, 2018.

561 Benjamin Billot, Douglas N Greve, Oula Puonti, Axel Thielscher, Koen Van Leemput, Bruce Fischl,
562 Adrian V Dalca, Juan Eugenio Iglesias, et al. Synthseg: Segmentation of brain mri scans of any
563 contrast and resolution without retraining. *Medical image analysis*, 86:102789, 2023.

564 Hyungjin Chung, Jeongsol Kim, Michael Thompson Mccann, Marc Louis Klasky, and Jong Chul Ye.
565 Diffusion posterior sampling for general noisy inverse problems. In *The Eleventh International
566 Conference on Learning Representations*, 2023. URL <https://openreview.net/forum?id=OnD9zGAGT0k>.

567 Roy De Maesschalck, Delphine Jouan-Rimbaud, and Désiré L Massart. The mahalanobis distance.
568 *Chemometrics and intelligent laboratory systems*, 50(1):1–18, 2000.

569 Bram de Wilde, Max T Rietberg, Guillaume Lajoinie, and Jelmer M Wolterink. Steerable anatomical
570 shape synthesis with implicit neural representations. *arXiv preprint arXiv:2504.03313*, 2025.

571 Yang Deng, Ce Wang, Yuan Hui, Qian Li, Jun Li, Shiwei Luo, Mengke Sun, Quan Quan, Shuxin
572 Yang, You Hao, et al. Ctspine1k: A large-scale dataset for spinal vertebrae segmentation in
573 computed tomography. *arXiv preprint arXiv:2105.14711*, 2021.

574 Neel Dey, Benjamin Billot, Hallee E. Wong, Clinton Wang, Mengwei Ren, Ellen Grant, Adrian V
575 Dalca, and Polina Golland. Learning general-purpose biomedical volume representations using
576 randomized synthesis. In *The Thirteenth International Conference on Learning Representations*,
577 2025. URL <https://openreview.net/forum?id=xOmC5LiVuN>.

578 Haoran Dou, Seppo Virtanen, Nishant Ravikumar, and Alejandro F Frangi. A generative shape
579 compositional framework: Towards representative populations of virtual heart chimaeras. *arXiv
580 preprint arXiv:2210.01607*, 2022.

581 Pan Du, Mingqi Xu, Xiaozhi Zhu, and Jian-xun Wang. Hug-vas: A hierarchical nurbs-based genera-
582 tive model for aortic geometry synthesis and controllable editing. *arXiv preprint arXiv:2507.11474*,
583 2025.

584 Yilun Du, Conor Durkan, Robin Strudel, Joshua B Tenenbaum, Sander Dieleman, Rob Fergus, Jascha
585 Sohl-Dickstein, Arnaud Doucet, and Will Sussman Grathwohl. Reduce, reuse, recycle: Composi-
586 tional generation with energy-based diffusion models and mcmc. In *International conference on
587 machine learning*, pp. 8489–8510. PMLR, 2023.

594 Dave Epstein, Allan Jabri, Ben Poole, Alexei Efros, and Aleksander Holynski. Diffusion self-
 595 guidance for controllable image generation. *Advances in Neural Information Processing Systems*,
 596 36:16222–16239, 2023.

597

598 Enrico Fabris, Balasz Berta, Tomasz Roleder, Renicus S Hermanides, Alexander JJ IJsselmuiden,
 599 Floris Kauer, Fernando Alfonso, Clemens Von Birgelen, Javier Escaned, Cyril Camaro, et al. Thin-
 600 cap fibroatheroma rather than any lipid plaques increases the risk of cardiovascular events in dia-
 601 betic patients: Insights from the combine oct–ffr trial. *Circulation: Cardiovascular Interventions*,
 602 15(5):e011728, 2022.

603

604 Weixi Feng, Chao Liu, Sifei Liu, William Yang Wang, Arash Vahdat, and Weili Nie. Blobgen-
 605 vid: Compositional text-to-video generation with blob video representations. *arXiv preprint*
 606 *arXiv:2501.07647*, 2025.

607

608 Virginia Fernandez, Walter Hugo Lopez Pinaya, Pedro Borges, Petru-Daniel Tudosiu, Mark S
 609 Graham, Tom Vercauteren, and M Jorge Cardoso. Can segmentation models be trained with fully
 610 synthetically generated data? In *Simulation and Synthesis in Medical Imaging: 7th International*
 611 *Workshop, SASHIMI 2022, Held in Conjunction with MICCAI 2022, Singapore, September 18,*
 612 *2022, Proceedings*, pp. 79–90. Springer, 2022.

613

614 Virginia Fernandez, Walter Hugo Lopez Pinaya, Pedro Borges, Mark S Graham, Petru-Daniel Tudosiu,
 615 Tom Vercauteren, and M Jorge Cardoso. Generating multi-pathological and multi-modal images
 616 and labels for brain mri. *Medical Image Analysis*, 97:103278, 2024.

617

618 Jean Feydy, Thibault Séjourné, François-Xavier Vialard, Shun-ichi Amari, Alain Trouve, and Gabriel
 619 Peyré. Interpolating between optimal transport and mmd using sinkhorn divergences. In *The 22nd*
 620 *International Conference on Artificial Intelligence and Statistics*, pp. 2681–2690, 2019.

621

622 Anthony A Gatti, Louis Blankemeier, Dave Van Veen, Brian Hargreaves, Scott L Delp, Garry E
 623 Gold, Feliks Kogan, and Akshay S Chaudhari. Shapemed-knee: A dataset and neural shape model
 624 benchmark for modeling 3d femurs. *medRxiv*, 2024.

625

626 Vivek Gopalakrishnan and Polina Golland. Fast auto-differentiable digitally reconstructed radiographs
 627 for solving inverse problems in intraoperative imaging. In *Workshop on Clinical Image-Based*
 628 *Procedures*, pp. 1–11. Springer, 2022.

629

630 Vivek Gopalakrishnan, Neel Dey, and Polina Golland. Intraoperative 2d/3d image registration via
 631 differentiable x-ray rendering. In *Proceedings of the IEEE/CVF Conference on Computer Vision*
 632 *and Pattern Recognition*, pp. 11662–11672, 2024.

633

634 Shoaib A. Goraya, Shengzhe Ding, Mariam K. Arif, Hyunjoon Kong, and Arif Masud. Effect of
 635 circadian rhythm modulated blood flow on nanoparticle based targeted drug delivery in virtual in
 636 vivo arterial geometries. *Brain Multiphysics*, 7:100105, 2024. ISSN 2666-5220. doi: <https://doi.org/10.1016/j.brain.2024.100105>. URL <https://www.sciencedirect.com/science/article/pii/S2666522024000169>.

637

638 Uxio Hermida, Milou PM van Poppel, Malak Sabry, Hamed Keramati, Johannes K Steinweg, John M
 639 Simpson, Trisha V Vigneswaran, Reza Razavi, Kuberan Pushparajah, David FA Lloyd, et al. The
 640 onset of coarctation of the aorta before birth: Mechanistic insights from fetal arch anatomy and
 641 haemodynamics. *Computers in Biology and Medicine*, 182:109077, 2024.

642

643 Amir Hertz, Or Perel, Raja Giryes, Olga Sorkine-Hornung, and Daniel Cohen-Or. Spaghetti: Editing
 644 implicit shapes through part aware generation. *ACM Transactions on Graphics (TOG)*, 41(4):
 645 1–20, 2022.

646

647 Jonathan Ho and Tim Salimans. Classifier-free diffusion guidance. *arXiv preprint arXiv:2207.12598*,
 648 2022.

649

650 SY Ho and P Nihoyannopoulos. Anatomy, echocardiography, and normal right ventricular dimensions.
 651 *Heart*, 92(suppl 1):i2–i13, 2006.

648 Karim Kadry, Max L Olender, David Marlevi, Elazer R Edelman, and Farhad R Nezami. A platform
 649 for high-fidelity patient-specific structural modelling of atherosclerotic arteries: from intravascular
 650 imaging to three-dimensional stress distributions. *Journal of the Royal Society Interface*, 18(182):
 651 20210436, 2021.

652 Karim Kadry, Shreya Gupta, Farhad R Nezami, and Elazer R Edelman. Probing the limits and
 653 capabilities of diffusion models for the anatomic editing of digital twins. *npj Digital Medicine*, 7
 654 (1):1–12, 2024.

655 Karim Kadry, Shreya Gupta, Jonas Sogbadji, Michiel Schaap, Kersten Petersen, Takuya Mizukami,
 656 Carlos Collet, Farhad R Nezami, and Elazer R Edelman. A diffusion model for simulation ready
 657 coronary anatomy with morpho-skeletal control. In *European Conference on Computer Vision*,
 658 pp. 396–412. Springer, 2025.

659 Soonpil Kang, JaeHyuk Kwack, and Arif Masud. Variational coupling of non-matching discretizations
 660 across finitely deforming fluid–structure interfaces. *International journal for numerical methods
 661 in fluids*, 94(6):678–718, 2022.

662 Tero Karras, Miika Aittala, Timo Aila, and Samuli Laine. Elucidating the design space of diffusion-
 663 based generative models. *arXiv preprint arXiv:2206.00364*, 2022.

664 Fanwei Kong, Sascha Stocker, Perry S Choi, Michael Ma, Daniel B Ennis, and Alison L Marsden.
 665 *Sdf4chd: Generative modeling of cardiac anatomies with congenital heart defects*. *Medical Image
 666 Analysis*, 97:103293, 2024a.

667 Fanwei Kong, Sascha Stocker, Perry S Choi, Michael Ma, Daniel B Ennis, and Alison L Marsden.
 668 *Sdf4chd: Generative modeling of cardiac anatomies with congenital heart defects*. *Medical Image
 669 Analysis*, 97:103293, 2024b.

670 Juil Koo, Seungwoo Yoo, Minh Hieu Nguyen, and Minhyuk Sung. Salad: Part-level latent diffu-
 671 sion for 3d shape generation and manipulation. In *Proceedings of the IEEE/CVF International
 672 Conference on Computer Vision*, pp. 14441–14451, 2023.

673 Tuomas Kynkänniemi, Tero Karras, Samuli Laine, Jaakko Lehtinen, and Timo Aila. Improved
 674 precision and recall metric for assessing generative models. *Advances in Neural Information
 675 Processing Systems*, 32, 2019.

676 Ali Madani, Ahmed Bakhaty, Jiwon Kim, Yara Mubarak, and Mohammad RK Mofrad. Bridging
 677 finite element and machine learning modeling: stress prediction of arterial walls in atherosclerosis.
 678 *Journal of biomechanical engineering*, 141(8):084502, 2019.

679 Masliza Mahmod, Kenneth Chan, Joao F Fernandes, Rina Ariga, Betty Raman, Ernesto Zacur, Ho-
 680 fon Royce Law, Marzia Rigolli, Jane M Francis, Sairia Dass, et al. Differentiating left ventricular
 681 remodeling in aortic stenosis from systemic hypertension. *Circulation: Cardiovascular Imaging*,
 682 17(8):e016489, 2024.

683 Brandon L Moore and Lakshmi Prasad Dasi. Coronary flow impacts aortic leaflet mechanics and
 684 aortic sinus hemodynamics. *Annals of biomedical engineering*, 43:2231–2241, 2015.

685 Jiteng Mu, Weichao Qiu, Adam Kortylewski, Alan Yuille, Nuno Vasconcelos, and Xiaolong Wang.
 686 *A-sdf: Learning disentangled signed distance functions for articulated shape representation*. In
 687 *Proceedings of the IEEE/CVF International Conference on Computer Vision*, pp. 13001–13011,
 688 2021.

689 Weili Nie, Sifei Liu, Morteza Mardani, Chao Liu, Benjamin Eckart, and Arash Vahdat. Compositional
 690 text-to-image generation with dense blob representations. *arXiv preprint arXiv:2405.08246*, 2024.

691 SA Niederer, Yasser Aboelkassem, Chris D Cantwell, Cesare Corrado, Sam Coveney, Elizabeth M
 692 Cherry, Tammo Delhaas, Flavio H Fenton, AV Panfilov, P Pathmanathan, et al. Creation and
 693 application of virtual patient cohorts of heart models. *Philosophical Transactions of the Royal
 694 Society A*, 378(2173):20190558, 2020.

702 Jonathan Pham, Sofia Wyetzner, Martin R Pfaller, David W Parker, Doug L James, and Alison L Mars-
 703 den. *svmorph: Interactive geometry-editing tools for virtual patient-specific vascular anatomies*.
 704 *Journal of Biomechanical Engineering*, 145(3):031001, 2023.

705 Jonathan Pham, Fanwei Kong, Doug L James, and Alison L Marsden. *Virtual shape-editing of*
 706 *patient-specific vascular models using regularized kelvinlets*. *IEEE Transactions on Biomedical*
 707 *Engineering*, 2024.

708 Mengyun Qiao, Kathryn A McGurk, Shuo Wang, Paul M Matthews, Declan P O'Regan, and Wenja
 709 Bai. *A personalized time-resolved 3d mesh generative model for unveiling normal heart dynamics*.
 710 *Nature Machine Intelligence*, pp. 1–12, 2025.

711 Robin Rombach, Andreas Blattmann, Dominik Lorenz, Patrick Esser, and Björn Ommer. *High-*
 712 *resolution image synthesis with latent diffusion models*. In *Proceedings of the IEEE/CVF*
 713 *Conference on Computer Vision and Pattern Recognition*, pp. 10684–10695, 2022.

714 Caroline H Roney, Marianne L Beach, Arihant M Mehta, Iain Sim, Cesare Corrado, Rokas Bendikas,
 715 Jose A Solis-Lemus, Orod Razeghi, John Whitaker, Louisa O'Neill, et al. *In silico comparison*
 716 *of left atrial ablation techniques that target the anatomical, structural, and electrical substrates of*
 717 *atrial fibrillation*. *Frontiers in physiology*, 11:1145, 2020.

718 Federica Sacco, Bruno Paun, Oriol Lehmkuhl, Tinen L Iles, Paul A Iaizzo, Guillaume Houzeaux,
 719 Mariano Vázquez, Constantine Butakoff, and Jazmin Aguado-Sierra. *Left ventricular trabeculations*
 720 *decrease the wall shear stress and increase the intra-ventricular pressure drop in cfd simulations*.
 721 *Frontiers in Physiology*, 9:458, 2018.

722 Ali Sarrami-Foroushani, Toni Lassila, Michael MacRaild, Joshua Asquith, Kit CB Roes, James V
 723 Byrne, and Alejandro F Frangi. *In-silico trial of intracranial flow diverters replicates and expands*
 724 *insights from conventional clinical trials*. *Nature communications*, 12(1):3861, 2021.

725 Hannes Stark, Bowen Jing, Tomas Geffner, Jason Yim, Tommi Jaakkola, Arash Vahdat, and
 726 Karsten Kreis. *Protcomposer: Compositional protein structure generation with 3d ellipsoids*.
 727 In *The Thirteenth International Conference on Learning Representations*, 2025. URL <https://openreview.net/forum?id=0ctvBgKFgc>.

728 Ross Straughan, Karim Kadry, Sahil A Parikh, Elazer R Edelman, and Farhad R Nezami. *Fully*
 729 *automated construction of three-dimensional finite element simulations from optical coherence*
 730 *tomography*. *Computers in Biology and Medicine*, 165:107341, 2023.

731 Marco Viceconti, Luca Emili, Payman Afshari, Eulalie Courcelles, Cristina Curreli, Nele Famaey,
 732 Liesbet Geris, Marc Horner, Maria Cristina Jori, Alexander Kulesza, et al. *Possible contexts of*
 733 *use for in silico trials methodologies: a consensus-based review*. *IEEE Journal of Biomedical and*
 734 *Health Informatics*, 25(10):3977–3982, 2021.

735 Jakob Wasserthal, Hanns-Christian Breit, Manfred T Meyer, Maurice Pradella, Daniel Hinck, Alexander
 736 W Sauter, Tobias Heye, Daniel T Boll, Joshy Cyriac, Shan Yang, et al. *Totalsegmentator: robust*
 737 *segmentation of 104 anatomic structures in ct images*. *Radiology: Artificial Intelligence*, 5
 738 (5):e230024, 2023.

739 Jessica G Williams, David Marlevi, Jan L Bruse, Farhad R Nezami, Hamed Moradi, Ronald N
 740 Fortunato, Spandan Maiti, Marie Billaud, Elazer R Edelman, and Thomas G Gleason. *Aortic*
 741 *dissection is determined by specific shape and hemodynamic interactions*. *Annals of Biomedical*
 742 *Engineering*, 50(12):1771–1786, 2022.

743 Guandao Yang, Xun Huang, Zekun Hao, Ming-Yu Liu, Serge Belongie, and Bharath Hariharan.
 744 *Pointflow: 3d point cloud generation with continuous normalizing flows*. In *Proceedings of the*
 745 *IEEE/CVF international conference on computer vision*, pp. 4541–4550, 2019.

746 Qinxi Yu, Masoud Moghani, Karthik Dharmarajan, Vincent Schorp, William Chung-Ho Pan-
 747 itch, Jingzhou Liu, Kush Hari, Huang Huang, Mayank Mittal, Ken Goldberg, et al. *Orbit-*
 748 *surgical: An open-simulation framework for learning surgical augmented dexterity*. *arXiv preprint*
 749 *arXiv:2404.16027*, 2024.

756 8 APPENDIX
757758 8.1 OVERVIEW
759

- 760 • In Section 8.2, we provide details on dataset curation and processing.
- 761 • In Section 8.3, we provide implementation details for our autoencoder and diffusion model.
- 762 • In Section 8.4, we provide implementation details for our guidance algorithm.
- 763 • In Section 8.5, we provide implementation details for our conditional generation baselines.
- 764 • In Section 8.6, we provide further experimental details for evaluation and inference.
- 765 • In Section 8.7, we provide implementation details for our biomechanical simulations.
- 766 • In Section 8.8 we provide a dataset scaling analysis for our latent diffusion model.
- 767 • In Section 8.9 we provide qualitative results for a procedurally generated ellipsoid dataset.
- 768 • In Section 8.10 we provide an autoencoder reconstruction error analysis.
- 769 • In Section 8.11 we provide a scale-factor sweep analysis for target modification.
- 770 • In Section 8.12 we provide quantitative results demonstrating disentangled generation for
- 771 alternative geometric features derived from the second-order moment.
- 772 • In Section 8.13, we present additional morphological distribution plots that examine the
- 773 effect of guidance weight as well as the choice of control technique.

774 8.2 DATASETS
775

776 For our study, we construct four separate datasets of anatomical segmentations to qualitatively
777 demonstrate the flexibility of geometric guidance. These datasets represent 1) whole-heart cardiac
778 segmentations with great vessels, 2) the branched ascending aorta, 3) multi-vertebral spinal column,
779 and 4) the femoral condyle and articular cartilage. We primarily use the cardiac dataset for our
780 experiments.

781 For the cardiac dataset, we utilize TotalSegmentator v2 Wasserthal et al. (2023), with 596 cases
782 manually selected based on segmentation quality assessment. Cardiac structures including the
783 myocardium (Myo), left and right atria (LA & RA), left and right ventricles (LV & RV), aorta (Ao),
784 and pulmonary artery (PA) were segmented using a specialized TotalSegmentator model trained on
785 sub-millimeter resolution data. For the inferior vena cava (IVC), superior vena cava (SVC), and
786 pulmonary veins (PV), we retain the labels from the original dataset. To ensure anatomical validity, we
787 perform topological filtration on all structures except the pulmonary veins, where filtration involves
788 extracting only the largest connected component. The resulting segmentations are standardized by
789 resampling to a uniform voxel resolution of 2mm and subsequently cropped to a fixed range. The
790 crop center is determined from the union of all four chamber segmentations, and the crop size is 128^3
791 voxels.

792 For the aorta dataset, we extract labels directly from the original TotalSegmentator v2 Wasserthal
793 et al. (2023) segmentations, without applying a specialized model, resulting in 450 3D segmentations
794 manually selected based on segmentation quality assessment. The labels include the main aortic
795 trunk and the ascending branches, which comprise the brachiocephalic trunk (BCT), left common
796 carotid artery (LCCA), right common carotid artery (RCCA), left subclavian artery (LSCA), and
797 right subclavian artery (RSCA), for a total of 7 channels per segmentation. All segmentations are
798 resampled to an isotropic voxel size of 2 mm and cropped to a spatial size of 128^3 using a crop center
799 determined from the center of all combined tissues.

800 For the spinal dataset, we utilize the CTSpine1K dataset Deng et al. (2021) and extract all vertebral
801 body segmentations, resulting in 784 3D segmentations. The segmentations include 7 cervical
802 vertebrae (C1–C7), 12 thoracic vertebrae (T1–T12), and 5 lumbar vertebrae (L1–L5), for a total
803 of 25 channels per segmentation. To ensure spatial consistency and anatomical completeness, all
804 segmentations are first resampled to an isotropic voxel spacing of 1 mm. The center of the crop box
805 is determined from the union (voxelwise sum) of all vertebral structures in each scan, and a fixed
806 crop of 128^3 voxels is applied for each patient.

807 For the knee dataset, we utilize the ShapeMedKnee dataset Gatti et al. (2024) and extract 2000 3D
808 segmentations of the left knee. The segmentations include the femur (Fe) and articular cartilage (Ca),

810 resulting in 3 channels per segmentation. To ensure spatial consistency and anatomical completeness,
 811 all segmentations are first resampled to an isotropic voxel spacing of 1 mm. A fixed crop size of 128^3
 812 voxels is applied for each patient.
 813

814 8.3 LATENT DIFFUSION MODEL IMPLEMENTATION 815

816 For this study, we adapt the VAE and LDM architectures specified by Kadry et al. (2024). The VAE
 817 input and output channel counts are set to 11, corresponding to 10 distinct cardiac labels along with
 818 an additional channel for the background. The number of input channels for the LDM is set to 3 for
 819 unconditional sampling. The hyperparameters and training configuration for the VAE and LDM are
 820 listed in Table 2 and Table 3 respectively.
 821

822 Table 2: Autoencoder hyperparameters
 823

824 Hyperparameter	825 Value
826 lr	1×10^{-5}
827 Epochs	40
828 Batch Size	1
829 Num. Channels	[16,32,64]
830 Num. Res. Blocks	2
831 Downscaling Factor	4
832 Recon. Loss Weight	1
833 KL Weight	1×10^{-6}

834 Table 3: Diffusion model hyperparameters
 835

836 Hyperparameter	837 Value
Training	
838 lr	2.5×10^{-5}
839 Epochs	50
840 Batch Size	1
841 Num. Channels	[64, 128, 196]
842 Num. Res. Blocks	2
843 Num. Attn. Heads	1
844 Attn. Res.	8, 4, 2
845 σ_{data}	1
846 $p(\sigma)$ mean	1
847 $p(\sigma)$ std	1.2
Sampling	
848 σ_{\min}	1×10^{-2}
849 σ_{\max}	80
850 ρ	3

851 8.4 GEOMETRIC GUIDANCE IMPLEMENTATION 852

853 8.4.1 GEOMETRIC MOMENT COMPUTATION

854 To ensure that the extracted components yield interpretable moments, we require the voxel grid
 855 values to be softly binarized, with one tissue channel approaching 1 while the others are close to 0.
 856 To achieve this, we apply a softmax function with a temperature of 1. During the computation of
 857 geometric moments, we observed that segmentations that are empty or nearly empty, particularly
 858 those with small components, lead to unstable gradients that significantly degrade the quality of
 859 generation. This instability arises because the centroid and covariance loss calculations utilize mass
 860 in the denominator. To mitigate this issue, we introduce a small amount of noise to the mass term
 861 whenever it appears in the denominator, thereby stabilizing the overall process. After computing all
 862 moments, we normalize the mass term by the total number of voxels $N = HWD$ such that the term
 863 represents volume fraction. Unless stated otherwise, we use 50 denoising steps.
 864

864 8.4.2 GUIDANCE WEIGHT TUNING
865866 We determine the weight factors $\lambda = [\lambda_0, \lambda_1, \lambda_2]$ for our geometric loss through tuning each loss in
867 isolation. We tune for conditional fidelity while retaining reasonable generation quality metrics. The
868 final weight values can be seen in Table 4.
869870 Table 4: Geometric moment losses and their corresponding weight factors.
871

872 Guidance 873 Loss	874 Weight 875 Factor λ
875 $\mathcal{L}_{\text{size}}$	876 10^7
876 \mathcal{L}_{pos}	877 10^5
877 $\mathcal{L}_{\text{shape}}$	10^4

880 8.5 BASELINE METHODS IMPLEMENTATION
881

- 882 • **Explicit Conditioning:** To ensure that the elements of \mathcal{G}_{exp} are roughly between 0 and 1, we
883 min-max normalize the masses \mathcal{M} , centroids \mathcal{C} , and normalized covariances \mathcal{S}_n with values
884 calculated from the real dataset (Table 5). The LDM input channel count is increased to
885 accommodate the concatenated input. This method does not readily permit the use of dropout
886 to train a diffusion model in an unconditional manner because the null condition is defined as
887 zero—equivalent to the minimum moment values. We include explicit conditioning results
888 for guidance weights smaller than 0 in Figure 4 for completeness.
889
- 890 • **Cross-Attention Conditioning:** Our initial tokens consist of 13-dimensional vectors rep-
891 resenting the concatenation of mass \mathcal{M} , centroids \mathcal{C} , and normalized covariances \mathcal{S}_n . The
892 tokens are then min-max normalized similar to explicit conditioning and embedded into a
893 256 dimensional vector for cross-attention. To embed the component index, we use a linear
894 embedding layer. To embed the geometric moments, we use an MLP with three linear layers
895 and apply a ReLU operation after the first and second layers. Both embeddings are added
896 together and used to condition the U-Net with cross-attention, where we use 8 attention
897 heads. To enable unconditional generation, we randomly dropout each channel of $\mathcal{G}_{\text{cross}}$ with
898 a probability of 0.1.
899
- 900 • **Implicit Conditioning:** To compute the ellipsoidal distance map, we use the centroids \mathcal{C} and
901 non-normalized covariances \mathcal{S} for each component to compute the Mahalanobis distance
902 De Maesschalck et al. (2000) for each voxel position. We then apply a shifted sigmoid
903 transform—with a slope of -0.5 and a bias of 1 to constrain the outputs between 0 and
904 1, and subsequently concatenate the resulting grid to the latents. To enable unconditional
905 generation, we randomly dropout each channel of \mathcal{G}_{imp} with a probability of 0.1. One
906 limitation of this approach is that the target mass can only be targeted indirectly through the
907 non-normalized covariance term, which can be seen in the conditional fidelity plot for size
908 in Figure 4.
909

910 Table 5: Normalizing constants for geometric moments during explicit and cross-attention based
911 conditioning.
912

913 Geometric 914 Moment	915 Normalizing 916 Minimum	917 Normalizing 918 Maximum
915 \mathcal{M}	3.19×10^{-3}	1.3×10^{-2}
916 \mathcal{C}	0	1
917 \mathcal{S}	-1×10^{-4}	1×10^{-2}

918 8.6 ADDITIONAL EXPERIMENTAL DETAILS
919

920 • **Morphological evaluation metrics:** To compute the morphological metrics, the features
921 are normalized by the mean and standard deviation of the real data. To calculate precision
922 and recall, we use 5 neighbors.

923 • **Pointcloud evaluation metrics** To compute the point cloud metrics, we calculate MMD,
924 COV, and NNA for every tissue label using 256 points sampled using farthest point sampling.
925 The metrics are then averaged over the number of components. To compute the pointcloud
926 distances, we approximate Earth Mover’s Distance (EMD) through the Sinkhorn divergence
927 Feydy et al. (2019).

928 • **Disentangled Generation:** Disentangled generation is done by zeroing out the inactive loss
929 weights. Exact configuration details are shown in Table 6. We use 50 denoising steps for all
930 generated samples.

931 • **Compositional Generation:** Our compositional generation experiments vary the number of
932 constrained substructures. The exact labels used for each experiment are detailed in Table 7.
933 We use 100 denoising steps for all generated samples.

934
935 Table 6: Configuration details for the disentangled generation ablation study. Checkmarks \checkmark indicate
936 the associated weight factor λ_i is active while \times indicates the weighting factor is zeroed out.

938	Guidance Loss	λ_0	λ_1	λ_2
939	Uncond.	\times	\times	\times
940	$\mathcal{L}_{\text{size}}$	\checkmark	\times	\times
941	\mathcal{L}_{pos}	\times	\checkmark	\times
942	$\mathcal{L}_{\text{shape}}$	\times	\times	\checkmark
943	$\mathcal{L}_{\text{geom}}$	\checkmark	\checkmark	\checkmark

945
946 Table 7: Configuration details for the compositional generation study.

948	Substructures	Labels
949	0	None
950	1	RV
951	2	RV, RA
952	3	RV, RA, PA
953	6	RV, RA, PA, LV, LA, Ao

955 8.7 BIOMECHANICAL SIMULATION DETAILS
956

957 • **Biventricular Cropping:** As only myocardial tissue is available for the left ventricle, we
958 approximate an RV myocardial wall by dilating the RV cavity mask to a constant thickness
959 of 4 mm (2 voxels) corresponding to the clinical literature Ho & Nihoyannopoulos (2006).
960 To crop the left and right ventricles at the base of the heart, we define a vector from the LV
961 centroid to the LA centroid, and crop the ventricles by adjusting the position threshold along
962 the defined direction.

963 • **Tetrahedral Meshing and Processing:** The segmentation is then converted into a surface
964 mesh using marching cubes, with a voxel size of 2 mm. Tetrahedral mesh generation is
965 performed using the open-source software Gmsh and MeshLab. The three anatomical
966 models, large RV, baseline patient, and small RV (see Figure 11), are discretized into 39,780,
967 42,768, and 47,347 linear tetrahedral elements, respectively, with an average edge length of
968 2 mm.

969 • **Pressurization Simulation:** An in-house finite element method (FEM) solver, implemented
970 in Fortran with MPI, is used for the simulations. The solver is based on the variational
971 multiscale method, providing stabilized FEM formulations Goraya et al. (2024); Kang et al.
972 (2022). Simulation results are visualized using the open-source package ParaView.

972 The myocardium is modeled as a standard neo-Hookean material with a Young’s modulus of
 973 25 kPa and a Poisson’s ratio of 0.4. Physiological pressure loads of 12 mmHg and 6 mmHg
 974 were applied to the LV and RV endocardium, respectively, corresponding to normal diastolic
 975 blood pressure. To constrain rigid body motion, zero-displacement Dirichlet boundary
 976 conditions are imposed at the base of the heart, while a stress-free Neumann boundary
 977 condition is applied on the pericardium.

978 The nonlinear finite-deformation elasticity problem is then solved using the New-
 979 ton–Raphson (NR) method. A direct solver (**MUMPS**) is employed to solve the discretized
 980 algebraic system at each NR iteration, with a convergence tolerance set to 10^{-20} for the
 981 initial residual. Simulations are carried out on a cluster using 128 processors.

982

983 8.8 DATASET SCALING ANALYSIS

984

985 We aim to understand the effect of dataset size on both generation quality and conditional fidelity
 986 under guidance. To this end, we train four additional autoencoder–diffusion model pairs at different
 987 split sizes, using 20%, 40%, 60%, and 80% of the original training set, while keeping the validation
 988 set fixed across all models. As shown in Figure 13, generation-quality metrics improve as the training
 989 dataset size increases up to 40%. In contrast, conditional fidelity under geometric guidance remains
 990 approximately invariant across dataset sizes.

991

992 8.9 PARAMETRIC ELLIPSOID DATASET ANALYSIS

993

994 To further characterize our geometric guidance procedure in isolation from complex anatomical
 995 variation, we construct a toy dataset of 3D two-channel ellipsoidal label maps with varying sizes,
 996 shapes, and positions. To generate each voxel map, we sample the ellipsoidal radii uniformly from 0
 997 to 0.5, where 1 corresponds to the full length of the voxel map. We additionally sample Euler angles
 998 uniformly from 0 to 2π , and choose the centroid to lie anywhere within the voxel map such that the
 999 ellipsoid is not cropped by the voxel boundaries. We generate 800 training and 200 validation label
 maps.

1000

1001 We then train a latent diffusion model with double the number of base channels to accommodate
 1002 the large geometric variation in the dataset. We apply our geometric guidance method with centroid
 1003 and covariance loss weights multiplied by a factor of 10. As shown in Figure 14, our geometric
 1004 guidance framework can enforce precise geometric constraints on parametric ellipsoid geometries in
 a disentangled manner.

1005

1006 8.10 AUTOENCODER RECONSTRUCTION FIDELITY ANALYSIS

1007

1008 We aim to determine whether the conditional fidelity metrics and topological quality are lower-
 1009 bounded by the VAE reconstruction error. We first auto-encode 24 seed label maps and measure
 1010 conditional fidelity for size, position, and shape, as well as the Betti error for each anatomical structure.
 1011 We then sample 24 label maps over 50 diffusion steps with and without right-ventricular geometric
 1012 guidance. As summarized in Table 8, geometric guidance substantially improves conditional fidelity
 1013 relative to unconditional sampling, while the resulting errors for position and shape remain above the
 1014 VAE reconstruction error.

1015

1016 In terms of topology, we quantify quality using the Betti error, defined as the number of extra
 1017 connected components relative to the expected topology (e.g., if the aorta is expected to be a single
 1018 connected component but two are measured, the Betti error is 1). We observe that the VAE introduces
 1019 only a small number of topological defects, whereas the unconditional diffusion model produces
 1020 more frequent errors, especially for the aorta (Ao) and pulmonary artery (PA) labels. Finally, we find
 1021 that geometric guidance can further increase the Betti error, particularly for the PA and inferior vena
 1022 cava (IVC) labels.

1023

1024 8.11 EDITING SCALE FACTOR ANALYSIS

1025

1026 We investigate how far the target right-ventricular mass can be scaled while still producing plausible
 1027 samples. For each editing factor in $\{0.1, 0.5, 1.0, 2.0, 4.0\}$, we take 64 seed label maps, compute
 1028 the RV mass, multiply it by the editing factor, and use the scaled mass as the conditioning target

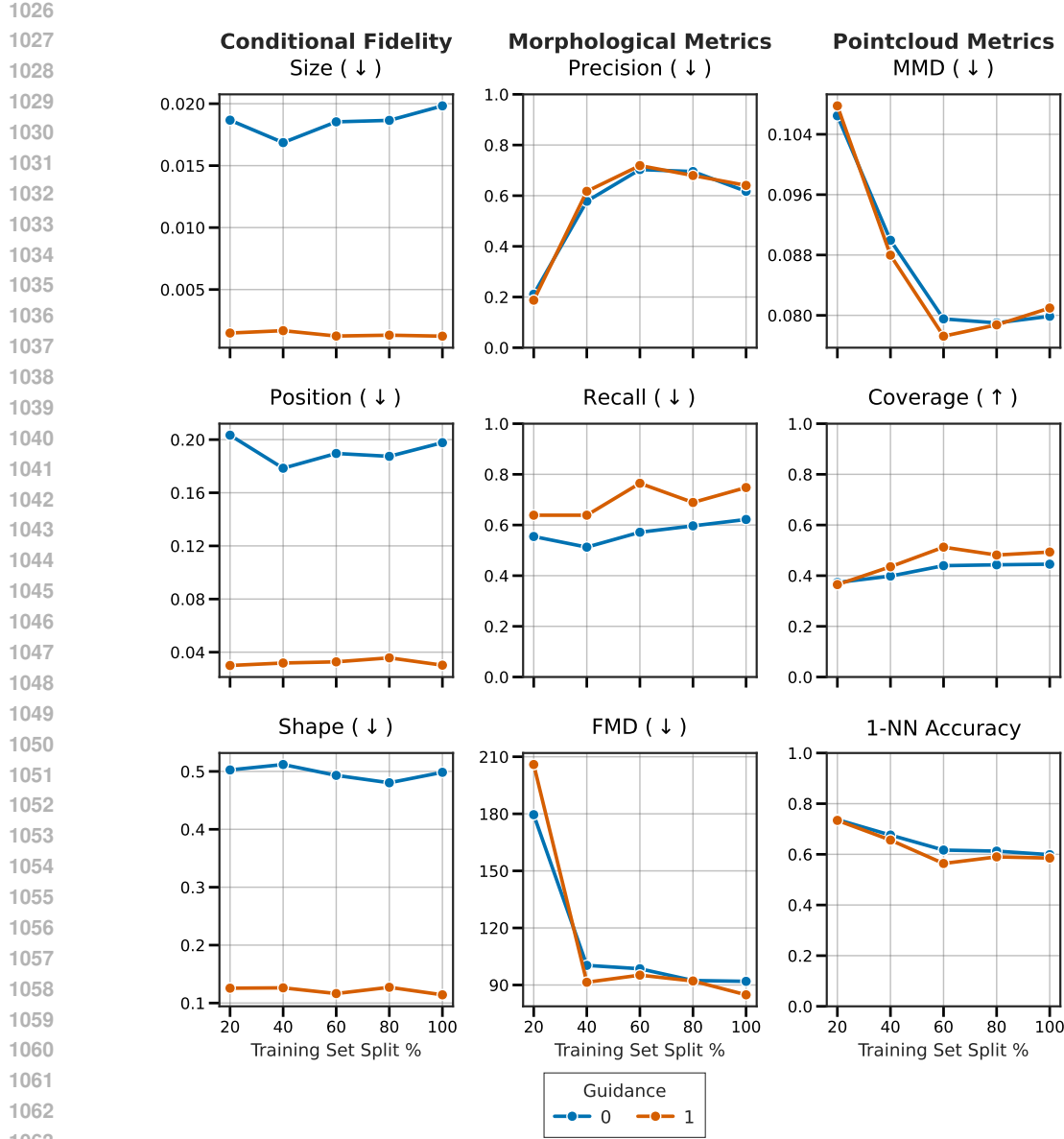


Figure 13: **Conditional fidelity is invariant to training set size, while generation quality metrics benefit from training set size up to a limit.** Line plots show conditional fidelity and generation quality for latent diffusion models trained on different-sized datasets. In this plot, the right ventricle is constrained.

for mass-only geometric guidance. As summarized in Table 9, decreasing the target mass (factors < 1) yields samples whose size error and distributional metrics remain close to the unedited case (factor = 1): size error increases moderately, and FMD and 1-NNA remain within the same order of magnitude as the baseline. In contrast, increasing the target mass beyond a factor of 2 leads to clear degradation: at a factor of 4, both the size error and FMD increase by more than one order of magnitude, and 1-NNA worsens, indicating that strong mass upscaling produces distorted label maps.

8.12 GEOMETRIC GUIDANCE WITH ALTERNATIVE MOMENT-FEATURES

In our main study, we demonstrated guidance by targeting the normalized second moment to control shape and orientation independently from size. We aim in this section to preliminarily demonstrate

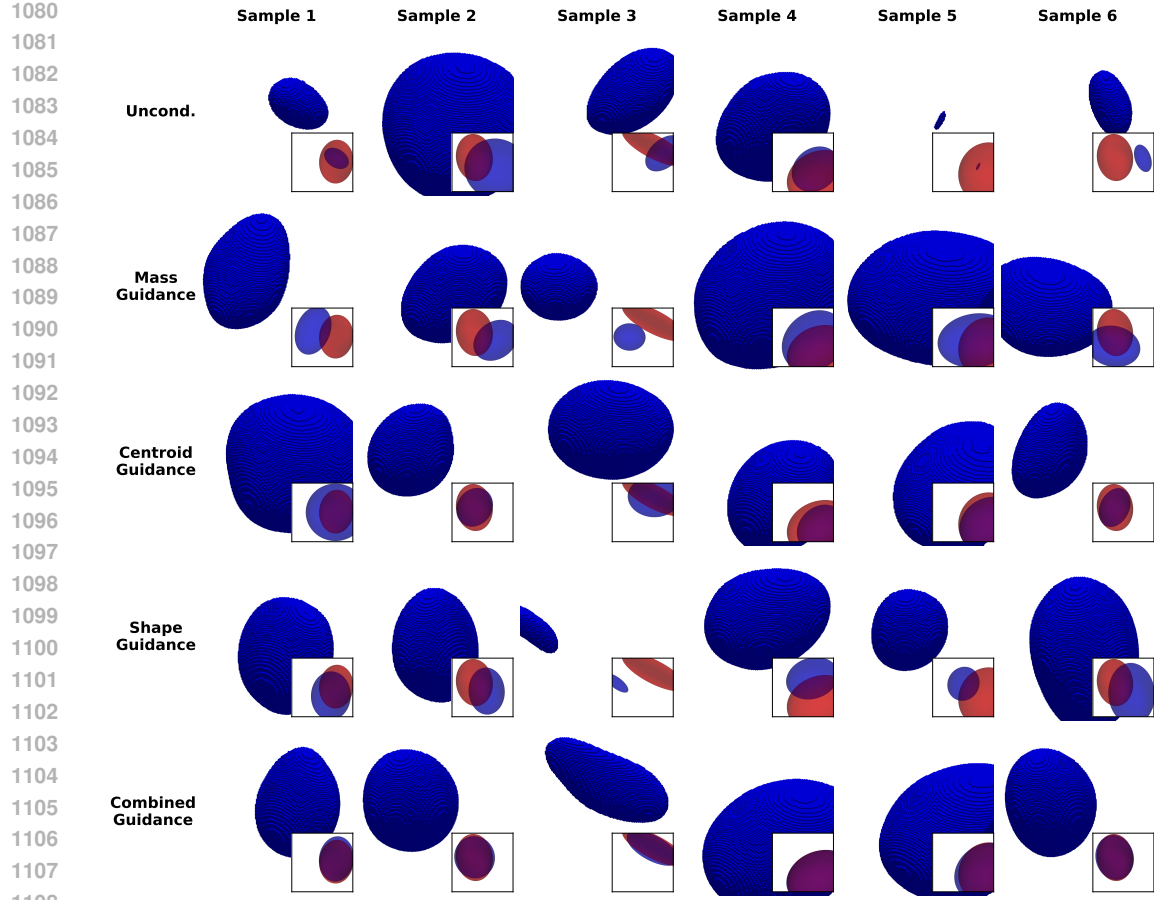


Figure 14: **Geometric guidance can control unconditional diffusion models of procedurally generated ellipsoids.** We generate ellipsoidal label maps with varying loss-function combinations to achieve disentangled control.

Table 8: Conditional fidelity and Betti error rates for reconstructed or synthetic label maps. Betti error is computed as the mean number of connected components minus 1. Values for size, position, and shape fidelity were multiplied by 1e5, 1e4, 1e4 respectively.

Method	Cond. Metrics			Connected Component Betti Error								
	Size	Pos.	Shape	Ao	PA	IVC	SVC	LA	RA	LV	RV	Myo
VAE Recon.	4.74	2.54	21.53	0.125	0.0	0.125	0.042	0.042	0.083	0.0	0.083	0.0
Unconditional	106.03	168.75	512.42	1.208	0.583	0.125	0.0	0.083	0.083	0.0	0.0	0.0
Guided	9.34	25.61	81.77	1.458	1.042	0.417	0.042	0.083	0.333	0.042	0.083	0.042

that we can achieve fine-grained disentangled control of second-moment derived attributes such as extent, stretch, and orientation. We first decompose the covariance matrix as follows:

$$\mathcal{S} = v\mathbf{U}\Lambda^n\mathbf{U}^T, \quad (6)$$

where we define the extent $v \in \mathbb{R}$ as the trace of the eigenvalue matrix $\Lambda \in \mathbb{R}^{3 \times 3}$, and normalize Λ by v to obtain the anisotropic stretch $\Lambda^n = \Lambda/v$. Finally, orientation is represented by the eigenvectors $\mathbf{U} \in \mathbb{R}^{3 \times 3}$ derived from the decomposition.

We then define three new geometric losses, which consist of MSE losses for extent and stretch, as well as a dot product loss for orientation.

$$\mathcal{L}_{\text{extent}} = \mathcal{L}_{\text{MSE}}(v, \bar{v}), \quad \mathcal{L}_{\text{stretch}} = \mathcal{L}_{\text{MSE}}(\Lambda^n, \bar{\Lambda}^n), \quad \mathcal{L}_{\text{orient}} = \mathcal{L}_{\text{dot}}(\mathbf{U}, \bar{\mathbf{U}}). \quad (7)$$

1134 Table 9: We generate label maps with mass-only geometric guidance applied to the right ventricle
 1135 and artificially changing the target mass derived from the seed label map.

1137 1138 1139 1140 1141 1142 1143 1144 1145 1146 1147 1148 1149 1150 1151 1152 1153 1154 1155 1156 1157 1158 1159 1160 1161 1162 1163 1164 1165 1166 1167 1168 1169 1170 1171 1172 1173 1174 1175 1176 1177 1178 1179 1180 1181 1182 1183 1184 1185 1186 1187	Cond. Metrics								Morph. Metrics			Pointcloud Metrics		
	Editing Factor	Size	FMD (↓)	Pr. (↑)	Re. (↑)	MMD (↓)	COV (↑)	1-NNA						
0.1	84.06	126.0	0.14	0.34		13.51	0.295	0.826						
0.5	19.95	59.6	0.55	0.50		10.51	0.406	0.713						
1.0	12.60	40.3	0.59	0.73		9.26	0.520	0.567						
2.0	18.55	167.5	0.16	0.84		11.08	0.430	0.745						
4.0	732.10	1690.0	0.00	0.97		26.81	0.273	0.926						

The dot product loss \mathcal{L}_{dot} is computed as the mean misalignment between corresponding eigenvectors from \mathbf{U} and $\bar{\mathbf{U}}$,

$$\mathcal{L}_{\text{dot}}(\mathbf{U}, \bar{\mathbf{U}}) = \frac{1}{3} \sum_{i=1}^3 (1 - |\mathbf{u}_i^\top \bar{\mathbf{u}}_i|^2), \quad (8)$$

where \mathbf{u}_i and $\bar{\mathbf{u}}_i$ denote the i -th columns of \mathbf{U} and $\bar{\mathbf{U}}$, respectively, and the absolute value enforces sign-invariance of eigenvector alignment.

With these losses, we conduct a disentangled generation experiment where we sample 32 label maps for each loss ablation setting, with the loss weightings detailed in Table 10. Conditional fidelity for extent and stretch is quantified using the mean absolute error, while conditional fidelity for orientation is quantified using the dot-product loss directly. As shown in Table 11, geometric guidance based on second-order derived features can be applied in a disentangled manner. For example, orientation-only guidance achieves a smaller orientation error while maintaining extent and stretch fidelity comparable to unconditional sampling.

Table 10: Second order moment losses and their corresponding weight factors.

1162 1163 1164 1165 1166 1167 1168 1169 1170 1171 1172 1173 1174 1175 1176 1177 1178 1179 1180 1181 1182 1183 1184 1185 1186 1187	Guidance Loss	Weight Factor λ
	$\mathcal{L}_{\text{extent}}$	10^5
	$\mathcal{L}_{\text{stretch}}$	10^4
	$\mathcal{L}_{\text{orient}}$	10^2

Table 11: We enable disentangled control over geometric features derived from decomposing the second moment into extent, stretch, and orientation. Conditional fidelity metrics for extent and stretch, as well as MMD values were multiplied by 1e3.

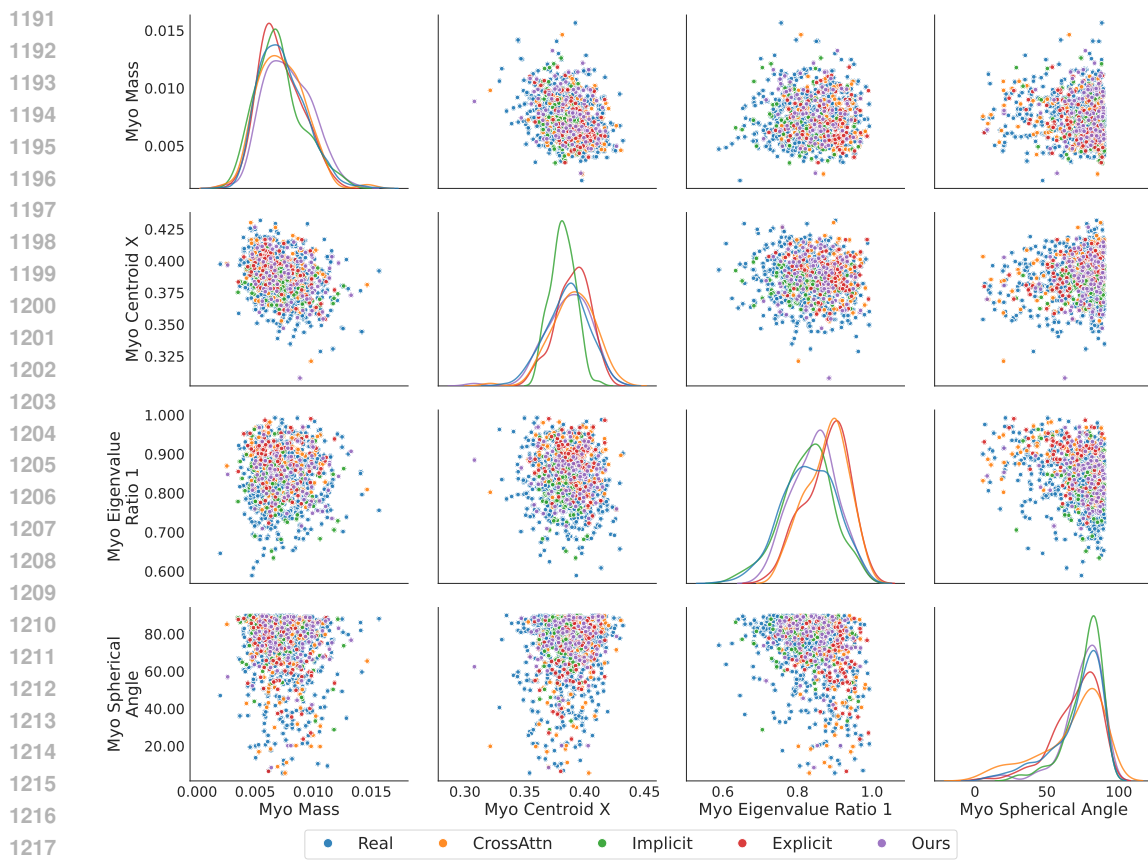
1173 1174 1175 1176 1177 1178 1179 1180 1181 1182 1183 1184 1185 1186 1187	Cond. Metrics			Morph. Metrics			Pointcloud Metrics			
	Method	Extent	Stretch	Orient.	FMD (↓)	Pr. (↑)	Re. (↑)	MMD (↓)	COV (↑)	1-NNA
None	2.14	42.30	0.21		67.63	0.44	0.80	10.22	0.484	0.563
Extent Only	1.42	41.85	0.20		61.99	0.50	0.78	10.12	0.459	0.566
Stretch Only	2.26	3.60	0.23		60.53	0.53	0.80	10.08	0.491	0.559
Orient Only	1.94	41.29	0.0064		60.81	0.59	0.77	10.08	0.525	0.564

8.13 MORPHOLOGICAL ANALYSIS

We represent size as the mass of each substructure. Position is represented by the centroid x-coordinate. To characterize shape, we extract the largest eigenvalue and its associated eigenvector from the covariance matrix. Orientation is represented by the polar angle of the principal axis (in spherical coordinates), while elongation is defined as the ratio between the largest eigenvalue and the second-largest eigenvalue.

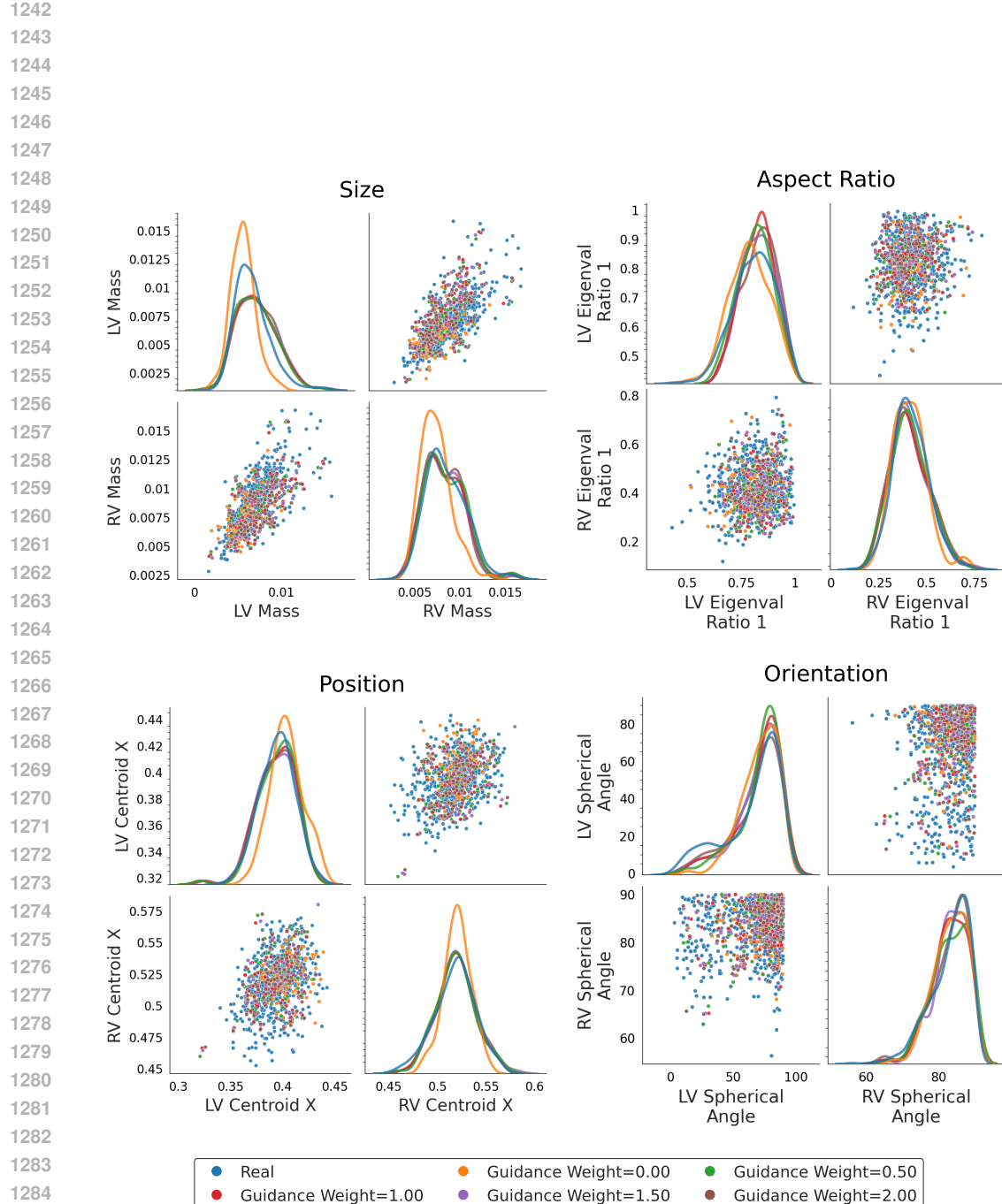
Additional morphological plots are presented below. In Figure 16, we show that geometric guidance better aligns the distribution of geometric features when comparing real and synthetic anatomies.

1188
 1189
 1190
 Figure 15 shows that all geometric-control methods can recapitulate the morphological distribution
 exhibited by the real data.



1219
 1220
 1221
 1222
 1223
 1224
 1225
 1226
 1227
 1228
 1229
 1230
 1231
 1232
 1233
 1234
 1235
 1236
 1237
 1238
 1239
 1240
 1241

Figure 15: Geometric guidance can help recapitulate morphological distributions. Pair plot shows kernel density estimate plots (diagonals) and pairwise scatterplots (off-diagonals) for various morphological metrics. We plot metrics for anatomies generated through conditional baselines and geometric guidance (ours). In this plot, the myocardium is being constrained.



1286 **Figure 16: Geometric guidance improves morphological distribution similarity between real and**
 1287 **synthetic anatomy.** Pair plot shows morphological relationships for mass (top left panel), centroid
 1288 (bottom left panel), normalized axis lengths (top right panel), and orientation (bottom right panel),
 1289 where the myocardium labels are being constrained. Diagonal plots show kernel density estimates
 1290 (LV vs RV), off-diagonal plots show pairwise scatterplots.

1291
 1292
 1293
 1294
 1295